Article

Growth of diamond in liquid metal at 1 atm pressure

https://doi.org/10.1038/s41586-024-07339-7

Received: 12 May 2023

Accepted: 20 March 2024

Published online: 24 April 2024

Check for updates

Yan Gong[1,2], Da Luo[1]✉, Myeonggi Choe[1,3], Yongchul Kim[1,2], Babu Ram[1], Mohammad Zafari[1], Won Kyung Seong[1]✉, Pavel Bakharev[1], Meihui Wang[1,7], In Kee Park[2], Seulyi Lee[4], Tae Joo Shin[5], Zonghoon Lee[1,3], Geunsik Lee[2] & Rodney S. Ruoff[1,2,3,6]✉

Natural diamonds were (and are) formed (thousands of million years ago) in the upper mantle of Earth in metallic melts at temperatures of 900–1,400 °C and at pressures of 5–6 GPa (refs. 1,2). Diamond is thermodynamically stable under high-pressure and high-temperature conditions as per the phase diagram of carbon[3]. Scientists at General Electric invented and used a high-pressure and high-temperature apparatus in 1955 to synthesize diamonds by using molten iron sulfide at about 7 GPa and 1,600 °C (refs. 4–6). There is an existing model that diamond can be grown using liquid metals only at both high pressure and high temperature[7]. Here we describe the growth of diamond crystals and polycrystalline diamond films with no seed particles using liquid metal but at 1 atm pressure and at 1,025 °C, breaking this pattern. Diamond grew in the subsurface of liquid metal composed of gallium, iron, nickel and silicon, by catalytic activation of methane and diffusion of carbon atoms into and within the subsurface regions. We found that the supersaturation of carbon in the liquid metal subsurface leads to the nucleation and growth of diamonds, with Si playing an important part in stabilizing tetravalently bonded carbon clusters that play a part in nucleation. Growth of (metastable) diamond in liquid metal at moderate temperature and 1 atm pressure opens many possibilities for further basic science studies and for the scaling of this type of growth.

Diamond, the hardest material known, possesses the highest atomic density and thermal conductivity, and a large band gap. When impurities such as N or Si (among other elements) are introduced, diamond shows vacancy centres (colour centres) that have sparked interest in magnetic sensing and quantum computing[8,9]. These attributes make diamond a versatile material with several realized or potential applications, including but not limited to very high-power electronics[10]. The properties of diamond[11] as well as its various applications (both synthetic and natural) have been extensively described in numerous reviews[12,13].

There exist two conventional methods for growing synthetic diamonds over a centimetre or larger scale. Chemical vapour deposition (CVD), including plasma-assisted CVD, thermally assisted (or hot-filament) CVD, reactive vapour deposition (for example, combustion methods) and various combinations of these, can deposit large-area single-crystal diamond as well as polycrystalline diamond films[14–16]. Another is high pressure and high temperature (HPHT) growth. Since 1955 (ref. 4) HPHT has been further developed and is now responsible for approximately 99% of the synthetic diamonds produced annually[17]. Carbon dissolved in liquid metal at a pressure of 5–6 GPa and a temperature of 1,300–1,600 °C will add to a seed diamond crystal, and these conditions are milder than for a pure carbon system[7,18]. It is reported that molten metal acts as a solvent for this dissolved carbon to diffuse to the diamond seed crystal—while not dissolving the seed crystal or the growing diamond[19]. By using a temperature gradient under a near-equilibrium process, single-crystal diamonds up to 1 cm^3 in size are said to be produced from diamond seed crystals by HPHT growth that takes 5–12 days (refs. 18,20,21). The growth of synthetic single-crystal diamonds by HPHT will always be limited to around a centimetre size because of the components used. We decided some years ago to explore alternative methods to produce synthetic diamonds under mild conditions, including decreasing (particularly) the pressure and also the temperature in the liquid metal as an interesting topic for fundamental science: the question is whether we can break the existing pattern.

Liquid metals have many outstanding physical and chemical properties[22,23]. Their liquid surface or interface offers great opportunities for catalysis[24,25]. However, all carbons made so far at 'low pressure' (such as 1 atm pressure or so) with liquid metals have been graphitic carbons (with very high sp^2-bonded carbon content)[26–31]. Recent studies reported that molten metal and/or alloys, including Ni, Pd and Pt dissolved in Sn, Pb, Bi, In or Ga, were able to efficiently convert methane

[1]Center for Multidimensional Carbon Materials (CMCM), Institute for Basic Science (IBS), Ulsan, Republic of Korea. [2]Department of Chemistry, Ulsan National Institute of Science and Technology (UNIST), Ulsan, Republic of Korea. [3]Department of Materials Science and Engineering, Ulsan National Institute of Science and Technology (UNIST), Ulsan, Republic of Korea. [4]UNIST Central Research Facilities (UCRF), Ulsan National University of Science and Technology (UNIST), Ulsan, Republic of Korea. [5]Graduate School of Semiconductor Materials and Devices Engineering, Ulsan National University of Science and Technology (UNIST), Ulsan, Republic of Korea. [6]School of Energy and Chemical Engineering, Ulsan National Institute of Science and Technology (UNIST), Ulsan, Republic of Korea. [7]Present address: State Key Laboratory of Materials Processing and Die & Mould Technology, School of Materials Science and Engineering, Huazhong University of Science and Technology, Wuhan, China. ✉e-mail: luodarhoda@gmail.com; one2rang@gmail.com; ruofflab@gmail.com

to hydrogen and (sp^2-bonded) solid carbon by lowering the activation barrier of breaking the C–H bond[28]. Monolayer or multilayer graphene was reported to be deposited either at the surface of Ga or at the interface between Ga and a substrate when methane was used as the carbon precursor[27]. Polymer films that normally do not 'graphitize' were reported to be converted to graphitic carbon at low temperature when contacted by Ga and several alloys[29]. Carbon dioxide was reported to be efficiently converted to (sp^2-bonded) solid carbon through bubbling into the eutectic alloy of gallium and indium at near room temperature[31]. For molten metals with moderate to relatively high solubility (such as iron, nickel and cobalt), only graphite or graphitic carbons are reportedly formed (and/or carbides) with them[32–36].

We discovered that liquid metal can be used to grow diamond at low pressure. We find that diamond can be grown at the interface of liquid metal and a graphite crucible (and when the interface of the liquid metal is with highly oriented pyrolytic graphite (HOPG) or 'EDM-3 Poco Graphite' or pyrolytic boron nitride (PBN), each as a thin sheet of material placed at the bottom of the graphite crucible).

Our growth of diamond on or in liquid metal at room pressure and modest temperature suggests that a variety of liquid metals (for example, indium, tin, lead, mercury and bismuth) can act as solvents and perhaps as catalysts as well. Many other elements can be added to these liquid metals; we suggest this will probably result in the synthesis of diamond by nucleation and growth in other liquid metals or at their interface with other materials. Solid carbon and many other gas-phase precursors than methane (for example, acetylene, ethylene and allene) can also act as a precursor for the growth.

Diamond growth in liquid metal at 1 atm

Liquid metal containing Ga, Ni, Fe and Si was used for the growth of diamonds. We used a custom-built cold-wall vacuum system that can rapidly heat and cool the metal (Fig. 1a, Supplementary Tables 1 and 2 and Supplementary Figs. 1–3). A graphite crucible is Joule-heated by electrical current (Supplementary Fig. 1), with temperature controlled by using a pyrometer (Fig. 1b, top). Figure 1b (bottom) shows the mixture of liquid Ga, and Ni and Fe ingots, and a small piece of Si wafer on the bottom cavity in the crucible before heating. A typical growth run was done with the pyrometer reading 1,175 °C in methane (CH_4) and hydrogen (H_2) at 760 torr. Ni, Fe and Si dissolve entirely into the liquid gallium forming a molten (liquid) metal.

Diamonds typically grew in the central region of the bottom surface of this liquid metal alloy, at its interface with either the bottom of the cavity of the graphite crucible or with thin pieces of HOPG or EDM-3 Poco Graphite or PBN (Methods) that we placed at the bottom of the crucible cavity to explore the potential role of different interfaces. A parametric study was undertaken in which these parameters were varied: growth temperature; the concentrations of Ni, Fe, and Si in liquid Ga (and thus also of Ga); and the methane to hydrogen ratio (Supplementary Figs. 4–12 and the discussion on the role of H_2 in Supplementary Information). We found diamonds were grown for the pyrometer reading from 1,165 °C to 1,190 °C and that these diamonds grew most abundantly for a 77.75/11.0/11.0/0.25 mix (atomic percentages) of Ga/Ni/Fe/Si at 1,175 °C during exposure to a gas mixture of methane and hydrogen at 760 torr that we refer to as an 'optimized growth condition' for growing diamonds and that was used for further studies of the growth. When $^{13}CH_4$ was substituted for normal methane, regions with ^{13}C-pure diamonds could be found. Deuterium gas was also used, suggesting that there is hydrogen present in the subsurface of the liquid metal and our as-grown diamond surfaces are hydrogen-terminated (Supplementary Figs. 13–15).

A typical growth result using the optimized growth condition is shown in Fig. 1c. Diamonds were found on the bottom surface of the solidified Ga–Fe–Ni–Si alloy piece and had rainbow colours to the eye (Fig. 1c); these regions contained diamonds (which were unequivocally identified as diamond by Raman spectroscopy, transmission electron microscopy (TEM) and X-ray diffraction (XRD); by observation of the negatively charged silicon-vacancy (SiV^-) centre in diamond; and by observation of only sp^3-bonded carbon by X-ray photoelectron spectroscopy (XPS)). As mentioned, diamonds nucleate and grow in the centre region but not in other regions (many diamond crystals are embedded in the solidified liquid metal surface); we suggest growth occurs in this region because the temperature of this centre region (about 1,025 °C) is the lowest in the liquid metal in the cavity (Supplementary Table 1 and Supplementary Fig. 2), and this plays a part in nucleation (and then growth) happening there. The diamond size and areal density were the highest in the central part of this 'diamond region', and both are reduced as we progress towards the outermost part of this region (Supplementary Fig. 16). In our many runs, diamonds were found only at the bottom surface of the solidified liquid metal piece (we did not find diamonds on, or embedded in, the four sides of the metal piece or its top surface).

For growth times of 15 min and 30 min, we find that many diamond crystals are partially submerged in the solidified liquid metal piece having a small portion projecting out of the metal surface (Fig. 1d,e and Supplementary Fig. 17). We note this strongly suggests that nucleation and growth of diamonds occur subsurface. Island regions formed by the merging of diamond crystals and with a size of a few microns were observed for the 60-min growth run (Fig. 1f and Supplementary Fig. 18), probably because of the increased density and larger size of the diamond crystals when the growth time is increased. For a growth time of 150 min, a nearly continuous diamond film was formed (Fig. 1g). We note that there were a few gaps in the diamond film region (Supplementary Fig. 19). Scanning electron microscopy (SEM) images of the as-grown diamond with growth times of 15 min, 30 min and 60 min were acquired at 50.0° tilt and are shown in Supplementary Fig. 20. When observed in an optical microscope, the continuous film shows various colours, including red, yellow and green (Fig. 1h). We note that for growth times longer than 150 min, the thickness and morphology of diamond film did not change (Supplementary Figs. 21 and 22).

Characterization of diamond

The as-grown diamond film can be delaminated and is readily transferrable to other substrate surfaces by dissolving the metal alloy piece using HCl(aq) solution (Methods). The back side of the transferred film (that was interfaced to the liquid metal and then the solidified liquid metal after cooling) is clean with only a tiny amount of Ga and Si detected by time-of-flight secondary ion mass spectrometry (TOF-SIMS) (Supplementary Fig. 23) and XPS (Supplementary Fig. 24). The optical images of the as-transferred diamond film on a Cu TEM grid coated with Quantifoil holey amorphous carbon film show it is transparent (Fig. 1i). Atomic force microscopy (AFM) of the as-transferred diamond film on the Cu TEM grid is shown in Fig. 1j, and the facets of the diamonds are clearly seen. The plane view TEM images of the as-transferred diamond film show diamond particles with different sizes and orientations and that there are, in some regions, gaps between the diamond particles (Supplementary Fig. 25). There was no graphitic structure or other carbon found in these gaps (Supplementary Fig. 26). The C1s XPS spectrum of an as-transferred film on a 300-nm SiO_2/Si wafer (Supplementary Fig. 27) has a single and symmetric peak at 285.1 eV correlating to sp^3-bonded carbon that suggests the film is diamond[37] (Supplementary Fig. 28). Synchrotron two-dimensional XRD (2D-XRD) pattern in grazing incidence mode of the same transferred diamond film suggests that it has a cubic structure (Fig. 1k), with (111), (220) and (311) diffraction Debye rings observed, suggesting that the as-transferred diamond film is polycrystalline. The polycrystalline diamond film is of high crystallinity showing the full width at half maximum of the Raman band (at 1,332 cm^{-1}) of about 15 cm^{-1} (Supplementary Fig. 29), and no Ga, Ni, Fe, and Si were detected

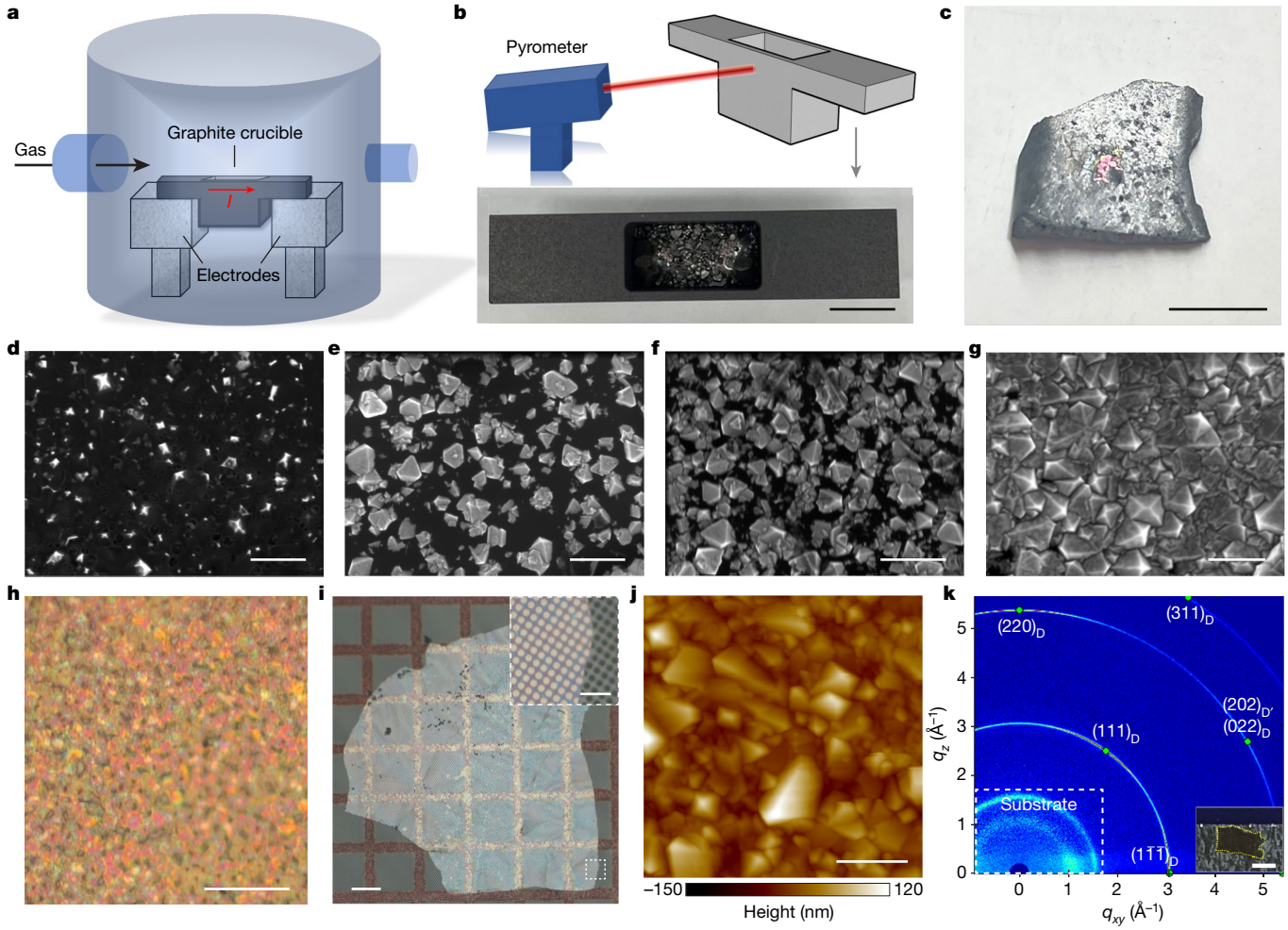

Fig. 1 | Synthesis of diamond on a liquid metal surface that is at an interface with graphite. a, Schematic of the experimental setup. A graphite crucible with cavity is the Joule-heated sample container in the cold-wall system. **b**, Schematic of the pyrometer and graphite crucible (top), and top view of the actual graphite crucible after filling the rectangular cavity with Ga, Ni, Fe and Si (bottom). **c**, As-grown diamond on the solidified liquid metal surface after a growth run. **d**–**g**, SEM images of diamond crystals after growth for 15 min (**d**), 30 min (**e**), 60 min (**f**) and 150 min (**g**). **h**, An optical image of the as-grown continuous diamond film on the solidified liquid metal surface. **i**, An optical image of the as-transferred diamond film on a Cu TEM grid coated with Quantifoil holey amorphous carbon film. Inset, a magnified optical image of the region inside the white dotted lines. Scale bar, 10 μm. **j**, AFM topographic image of the as-transferred diamond film on the Cu TEM grid. **k**, 2D-XRD pattern of a transferred diamond film on a 300-nm SiO_2/Si wafer. The dotted rectangle shows the region from the Si substrate and/or double-sided tape. Inset, a photograph of the transferred diamond film (yellow dotted area) adhered to the wafer with a double-sided tape. Scale bars, 1 cm (**b**); 5 mm (**c**); 500 nm (**d**–**g**); 20 μm (**h**); 50 μm (**i**); 500 nm (**j**); and 1 mm (**k**, inset).

in the film even to 50 nm depth by using TOF-SIMS depth profiling (Supplementary Fig. 30).

We used $^{13}CH_4$ (99 at% ^{13}C) instead of normal methane (98.9 at% ^{12}C) for some growth runs. We label the as-grown samples as ^{13}C-D150-GC for a 150-min growth run, for the configuration in which the entire bottom surface of the crucible cavity was contacted with liquid metal (Fig. 2a). A typical Raman spectrum acquired on ^{13}C-D150-GC (Fig. 2b) showed diamond peaks at 1,283 cm^{-1} and 1,332 cm^{-1}, and graphite G band peaks at 1,521 cm^{-1} and 1,580 cm^{-1}, which are the Raman bands of essentially pure ^{13}C-labelled diamond (^{13}D) and normal diamond (^{12}D) (ref. 38), and the G bands of essentially pure ^{13}C-labelled graphite (^{13}G) and normal graphite (^{12}G) (ref. 39), respectively. This Raman spectrum can be rationalized by both the methane and the graphite crucible contributing carbon to the growth of diamond and graphite. With the observed much larger intensity of Raman ^{12}D and ^{12}G peaks compared with ^{13}D and ^{13}G peaks, the graphite crucible seems to contribute larger amounts of carbon for the growth of both diamond and graphite than methane.

The graphite crucible is composed of isotropic graphite. We asked whether different types of carbon (carbon material) or even other materials 'interfaced' with the liquid metal, influence diamond growth at this interface. We thus covered regions of the bottom of the cavity with flat (square or rectangular) pieces of different types of graphite than the crucible graphite including HOPG pieces (Supplementary Fig. 31) and EDM-3 Poco Graphite plates, and also a PBN plate (Supplementary Fig. 32), and here we present results obtained with EDM-3 Poco Graphite. Placing one piece of EDM-3 Poco Graphite plate, or a stack of 10 of them, on the bottom surface of the cavity before adding the Ga, Fe, Ni and Si led to as-grown diamonds using $^{13}CH_4$ that we name ^{13}C-D150-EDM and ^{13}C-D150-SEDM (where S indicates stacked), (Fig. 2a). A typical Raman spectrum of ^{13}C-D150-EDM showed ^{13}D and ^{12}D peaks (and ^{13}G and ^{12}G peaks), but the intensities of the ^{12}D and ^{12}G peaks were substantially lower compared with those of the ^{13}D and ^{13}G peaks, showing the growth was mainly from $^{13}CH_4$ (that is, from methane). The spectrum of ^{13}C-D150-SEDM showed only ^{13}D and ^{13}G, thus all newly grown carbon was from $^{13}CH_4$. It is thus reasonable to assume that ^{12}D and ^{12}G Raman peaks observed in ^{13}C-D150-EDM were coming from carbon from the graphite crucible rather than from the inserted EDM-3 Poco Graphite plate: that is, the EDM-3 Poco Graphite plate does not contribute carbon to the growth of diamond and

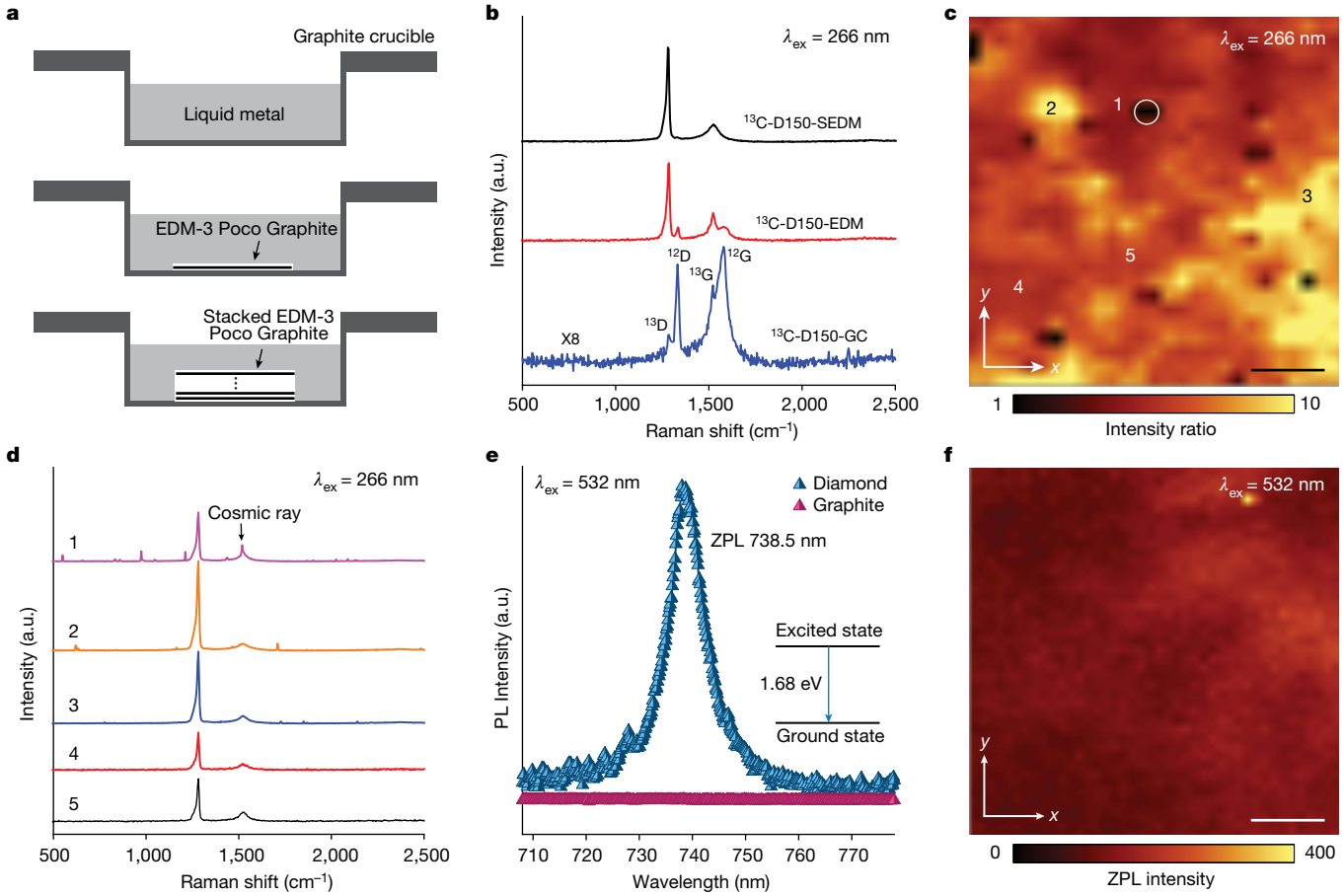

Fig. 2 | Characterization of ^{13}C-labelled as-grown diamond. a, Schematic of the three configurations used for growth. **b**, Raman spectra of ^{13}C-D150-GC, ^{13}C-D150-EDM, and ^{13}C-D150-SEDM. **c**, Raman map of I_D/I_G ratio of the region in ^{13}C-D150-SEDM. **d**, Raman spectra taken from the regions marked in **c**. The black spots in Fig. 2c are because of cosmic rays incident on the detector during mapping. **e**, ZPL peak of the as-grown diamonds compared with the as-grown graphite, excited by a 532-nm laser. **f**, Map of ZPL intensity of ^{13}C-D150-SEDM. a.u., arbitrary units; PL, photoluminescence. Scale bar, 10 μm (**c**,**f**).

graphite. The SEM images (Supplementary Fig. 33) showing that the surface of the graphite crucible is rougher and has larger pores present than EDM-3 Poco Graphite plate possibly rationalizes why some carbon in the crucible contributes to the growth of diamond and graphite.

The morphologies of ^{13}C-D150-GC, ^{13}C-D150-EDM and ^{13}C-D150-SEDM were quite similar (Supplementary Fig. 34). However, ^{13}C-D150-GC shows an intense Raman G band (Fig. 2b and Supplementary Fig. 35), suggesting the growth of more graphitic structures, compared with ^{13}C-D150-EDM (Fig. 2b and Supplementary Fig. 35) and ^{13}C-D150-SEDM (Fig. 2b–d and Supplementary Fig. 36) in which the C from methane (not the crucible carbon) dominates the growth. We note the I_D/I_G peak ratios for the growth with the same configurations with normal methane were quite similar to the peak ratios with $^{13}CH_4$ (Supplementary Fig. 37). This strongly indicates that methane is a better carbon source than the crucible carbon for the growth of high-quality diamond.

A typical photoluminescence spectrum of ^{13}C-D150-SEDM excited by a 532-nm laser is shown in Fig. 2e. The strong peak at 738.5 nm (1.679 eV) can be assigned to the zero-phonon line (ZPL) of the SiV^- colour centre[40]. A photoluminescence map of ZPL intensity over a 50 μm × 50 μm region showed this ZPL everywhere but with varying intensity (Fig. 2f).

Cross-sectional TEM analysis was used to study the atomic scale structure and elemental composition of the as-grown diamonds, as-grown graphite and different regions of the solidified liquid metal piece that were interfaced with these solid carbons. (We note that when graphite was present, graphite was formed primarily underneath the diamond. And the surface of the solidified liquid metal was not always flat. More details are provided in Supplementary Figs. 38–40). The cross-sectional specimens were prepared by focused ion beam (FIB) milling of the metal pieces obtained after growth runs of 150 min (D150) and 30 min (D30) (Methods). A typical large-area cross-sectional TEM image of D150 showed a diamond film at the solidified liquid metal surface (Fig. 3a). High-resolution TEM (HR-TEM) images of the diamond–metal interface show that the metal region has two different structures: one (labelled as M1) with a thickness of about 30 nm, and the other (labelled as M2) interfacing with M1 (Fig. 3b,c). The fast Fourier transform (FFT) patterns of M1 (top inset) and M2 (bottom inset) show that M1 is amorphous but M2 is crystalline (Fig. 3c). M2 shows a crystal lattice with clearly identifiable fringe spacings and without any structural defects or disorder. (Although the liquid metal cooled relatively rapidly due to turning off the electric current that had been driving the Joule heating, as described above, it did not freeze in the amorphous liquid metal state—crystallization of the interior of the liquid metal did occur in the few tens of seconds time scale of cooling—and without the formation of separated phases).

The near-surface solidified liquid metal region that is beneath the diamond film was studied by TEM energy-dispersive X-ray spectroscopy (TEM-EDS) line profiling, by scanning along the surface of M1 to the bulk of M2 (Fig. 3d), and we found a large amount of carbon (as atoms or very small clusters) is present in the M1 region. The carbon concentration decreases significantly from about 26.5 at% at the top surface to about 5.0 at% at a depth of approximately 40 nm, which is matched to the thickness of M1, and (seemingly) plateaus at about 3.0–5.0 at% for the M2 region. However, the M2 region might be carbon-free as

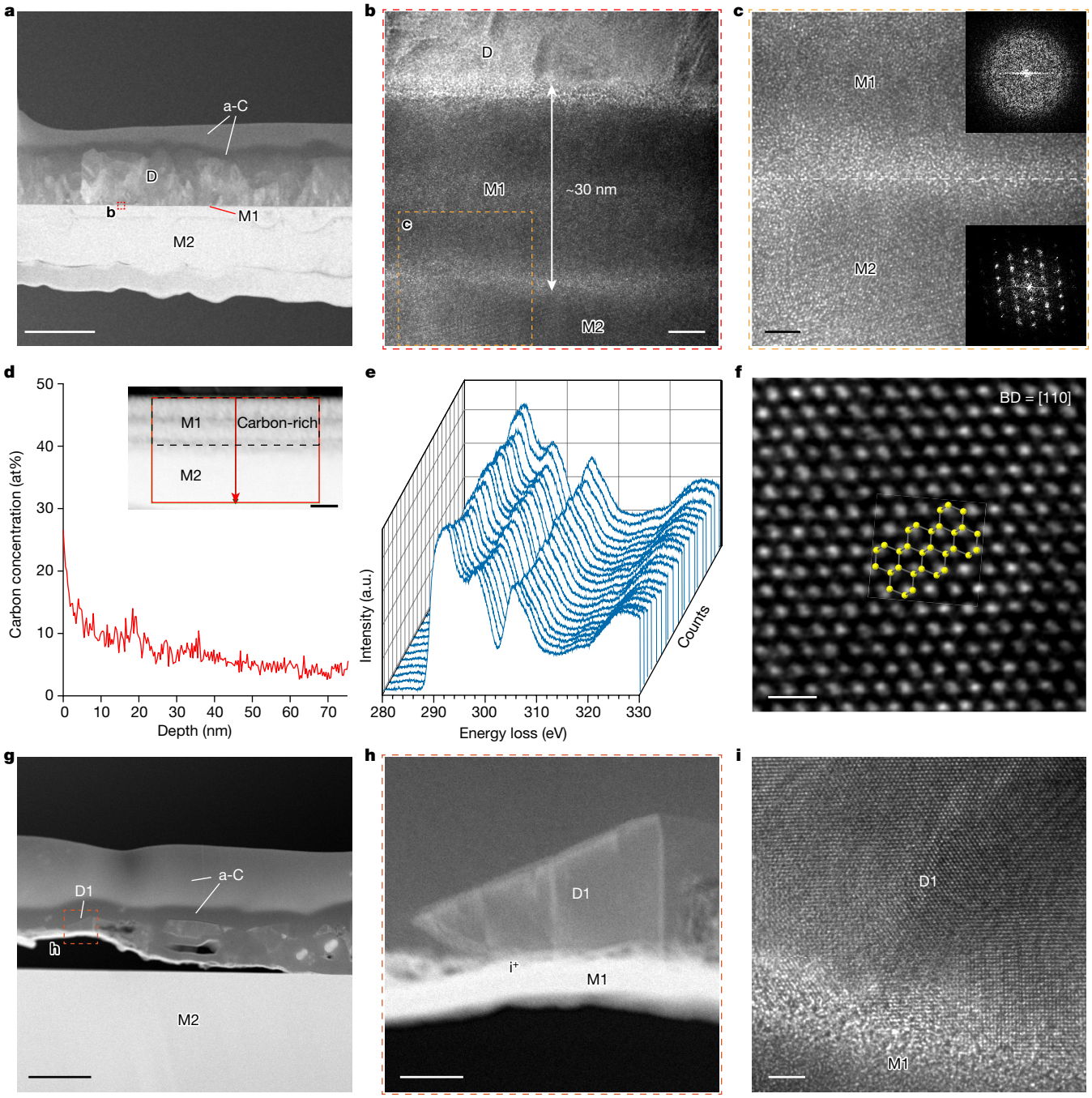

Fig. 3 | TEM data of cross-sectional samples prepared by SEM-FIB. **a**, Large-area cross-sectional TEM image of D150 with regions labelled a-C (amorphous carbon deposited for the SEM-FIB preparation (stabilization layer)); D (as-grown diamond film region); M1 (amorphous region present after solidification of liquid metal by rapid cooling); and M2 (crystalline region present after solidification of liquid metal by rapid cooling). **b**, HR-TEM image of the region enclosed in the red box in **a**, which includes D, M1 and M2. **c**, HR-TEM image of the region enclosed in the orange box in **b**. Inset, FFT pattern of the M1 region (top) and FFT pattern of the M2 region (bottom). **d**, TEM-EDS line profiling showing the carbon concentration of the region containing M1 and M2 of **a**. Inset, corresponding high-angle annular dark-field scanning transmission electron microscopy image showing the TEM-EDS line profiling region. **e**, TEM-EELS spectra of the D region in **a**. **f**, AR-TEM image of the D region in **b**, beam direction BD = [110]. The inset atomic model shows the C–C dumbbell units in diamond. **g**, Large-area cross-sectional TEM image of D30 with regions labelled a-C, D1, M1 and M2. Note that some regions of M1 peel away from M2 for some of our cross-section samples. **h**, TEM images of the regions enclosed in the red box in **g**. **i**, HR-TEM images of the regions marked by the black cross in **h**. a.u., arbitrary units. Scale bars, 500 nm (**a**,**g**); 5 nm (**b**); 2 nm (**c**,**i**); 20 nm (**d**); 0.5 nm (**f**); and 50 nm (**h**).

the detection limit of this method of identifying carbon concentration is around 2.0–4.0 at%. (But see the discussion about TOF-SIMS depth profiling data below that shows that at around 40 nm depth there can still be several at% C). Thus, a high percentage of carbon is dissolved in the M1 region of the (solidified) liquid metal before very rapid solidification but not to any, or to a lesser degree, in the bulk of the liquid metal. The presence of this high concentration of carbon in the M1 region is perhaps the reason for this region being amorphous.

Electron energy loss spectroscopy (EELS) spectra acquired from 20 randomly selected regions over the diamond region show only one major σ* peak around 292 eV (ref. 41) (Fig. 3e), suggesting the whole region is a uniform diamond film. An atomic resolution TEM (AR-TEM)

image obtained from the diamond region observed from the [110] zone axis (that is, the beam direction is [110]) shows the region is running parallel to the (110) diamond planes, with the C–C dumbbell units observed as bright spots in Fig. 3f (refs. 42,43).

We further imaged the interface between the diamond and the (solidified) liquid metal surface at the early stage of growth (D30). Isolated diamond crystals (for example, the one labelled as D1 in Fig. 3g) were found at the interface (Fig. 3g), and this agrees well with the SEM images (Fig. 1e). Amorphous M1 and crystalline M2 regions were again found underneath the diamond crystals (Fig. 3g,h and Supplementary Fig. 41; we note M1 in some regions was delaminated from M2). TEM-EDS maps of C, Ga, Ni, Fe and Si in the region in which D1 is located were obtained (Supplementary Fig. 42). TEM-EDS analysis shows the M1 region of D30 is carbon-rich (Supplementary Fig. 43).

D1 was found to be directly contacting the surface of the M1 region (Fig. 3h). The D1 crystal lattice fringes are not aligned with the same angle to the M1 surface (that is, there is not a constant orientation between the D1 lattice fringes and the M1 surface; Fig. 3i).

Mechanism of diamond growth

We did four growth runs with $^{13}CH_4$ and H_2 for 5 min, 10 min, 15 min and 150 min, and then studied the concentrations of carbon in the subsurface regions of the solidified liquid metal pieces (Supplementary Fig. 44), by using TOF-SIMS depth profiling. We found that the subsurface regions contain large concentrations of ^{13}C even to a depth of about 100 nm for all four runs, which agrees with our observation of the carbon-rich M1 region by TEM.

The carbon concentration at the region in which diamond normally grows (the central region at the bottom of the solidified liquid metal piece) for the 10-min run (about 65 at% at or near the surface) is much higher compared with that for the 15-min run (about 27 at% at or near the surface). No diamonds grew for the 10-min run but they grew for the 15-min run (Fig. 1d). We thus speculate that the concentration of subsurface carbon atoms at about 10 min is so high that the supersaturation is very close to nucleating diamonds. Nucleation occurs followed by rapid growth of diamond particles at some time between about 10 min and less than 15 min. We further note that for the 15-min run, the carbon concentration (for all depths from the surface to a depth of 300 nm) at the central region is higher compared with the region that is 5 mm away from the central region in which no diamond grew. This carbon concentration gradient is probably created by the temperature gradient (measured with inserted thermocouples as described in Supplementary Fig. 2) that rationalizes why diamonds grow in the central region. Under our growth conditions, in the central region when a very high concentration of carbon atoms is reached, diamond nuclei form and grow and are constantly fed new carbon by the surrounding, higher temperature regions (Supplementary Fig. 45); Si atoms play a part, as discussed further below.

We did theoretical simulations that suggest that methane is activated when adsorbing on the liquid metal surface (Supplementary Tables 3–4, Supplementary Figs. 46–48 and Supplementary Note 1). Our calculated change in endothermicity (compared with the gas-phase value of around 4.7 eV) for breaking the first C–H bond in CH_4 is very large, with some surface configurations showing exothermic reaction. Several experimental studies find activation energies for the rates of production of H_2 from methane with pure liquid gallium in our temperature range[44] or at lower temperatures[27] that range from 115.3 kJ mol^{-1} (ref. 44) to even much lower values[27].

We emphasize that Si plays an important part in our growth of diamond. Si was also relevant in our previous studies of homoepitaxial growth of diamond on single-crystal diamond[45]. Si (0.25 at%) used for our typical growth yields the diamonds of the largest crystal sizes at 150 min growth. Si (0.50 at% and 150 min growth) leads to a much higher density growth of diamonds of smaller crystal sizes (Supplementary Figs. 5 and 6). These two results along with our observation of the SiV^- colour centre, suggest Si plays a part in the nucleation of diamond; a higher nucleation density rationalizes the higher density growth of smaller diamonds at 0.50 at%. This is further suggested by our theoretical calculations that show that Si promotes the formation of, and also stabilizes, certain carbon clusters (likely to be the pre-nuclei for diamond growth) with mostly sp^3-like C bonding in liquid metals at our growth temperatures (Supplementary Figs. 49–56, Supplementary Note 2 and Supplementary Videos 1–8).

Furthermore, we found that the reduction of the amounts of Si in the subsurface (M1) region of liquid metal correlates with the cessation of diamond growth (Supplementary Fig. 57). Certain amounts of Si were consumed as diamond grows by forming the SiV^- colour centres (see further discussion in Supplementary Information and Supplementary Fig. 58). We found by AFM measurements essentially the same thickness diamond film for 300-min growth runs compared with 150-min growth runs (Supplementary Fig. 22). (That is, after about 150 min when Si is consumed to some extent, longer growth runs do not yield more diamond).

Conclusion

We discovered a method to grow diamonds at 1 atm pressure and under a moderate temperature by using a liquid metal alloy: this is unprecedented given the pattern that diamond can be grown only using liquid metals at high pressures in the range of 5–6 GPa and high temperatures. The diamond film contains SiV^- colour centres and can be transferred to any other substrate. We suggest that straightforward modifications could enable growing diamond over a very large area by using a larger surface or interface, by configuring heating elements to achieve a much larger potential growth region and by distributing carbon to the diamond growth region in some new ways.

The general approach of using liquid metals could accelerate and advance the growth of diamonds on a variety of surfaces, and perhaps facilitate the growth of diamond on small diamond (seed) particles. Considering the large number of possibilities for liquid metals, their eutectics (for example, using the Ga–In mixture as solvent or catalyst) (Supplementary Fig. 59), and the possibility of adding different amounts of various other elements that can act as catalysts (for example, dissolving some Co in Ga) (Supplementary Fig. 60), along with a wide range of possible carbon precursors apart from methane, the possibilities of exploring diamond growth with this type of approach seem promising.

Online content

Any methods, additional references, Nature Portfolio reporting summaries, source data, extended data, supplementary information, acknowledgements, peer review information; details of author contributions and competing interests; and statements of data and code availability are available at https://doi.org/10.1038/s41586-024-07339-7.

1. Haggerty, S. E. Diamond genesis in a multiply-constrained model. *Nature* **320**, 34–38 (1986).
2. Pal'yanov, Y. N., Sokol, A. G., Borzdov, Y. M., Khokhryakov, A. F. & Sobolev, N. V. Diamond formation from mantle carbonate fluids. *Nature* **400**, 417–418 (1999).
3. Bundy, F. P. et al. The pressure-temperature phase and transformation diagram for carbon; updated through 1994. *Carbon* **34**, 141–153 (1996).
4. Bundy, F. P., Hall, H. T., Strong, H. M. & Wentorfjun, R. H. Man-made diamonds. *Nature* **176**, 51–55 (1955).
5. Bovenkerk, H. P., Bundy, F. P., Hall, H. T., Strong, H. M. & Wentorf, R. H. Preparation of diamond. *Nature* **184**, 1094–1098 (1959).
6. Hazen, R. M. & Hazen, R. M. *The Diamond Makers* (Cambridge Univ. Press, 1999).
7. D'Haenens-Johansson, U. F. S., Butler, J. E. & Katrusha, A. N. Synthesis of diamonds and their identification. *Rev. Mineral. Geochem.* **88**, 689–753 (2022).
8. Doherty, M. W. et al. The nitrogen-vacancy colour centre in diamond. *Phys. Rep.* **528**, 1–45 (2013).
9. Ruf, M., Wan, N. H., Choi, H., Englund, D. & Hanson, R. Quantum networks based on color centers in diamond. *J. Appl. Phys.* **130**, 070901 (2021).

10. Shikata, S. Single crystal diamond wafers for high power electronics. *Diam. Relat. Mater.* **65**, 168–175 (2016).
11. Railkar, T. A. et al. A Critical Review of Chemical Vapor-Deposited (CVD) Diamond for Electronic Applications. *Crit. Rev. Solid State Mater. Sci.* **25**, 163–277 (2000).
12. Butler, J. E., Mankelevich, Y. A., Cheesman, A., Ma, J. & Ashfold, M. N. R. Understanding the chemical vapor deposition of diamond: recent progress. *J. Phys. Condens. Matter* **21**, 364201 (2009).
13. Yamasaki, S., Pobedinskas, P. & Nicley, S. S. Recent advances in diamond science and technology. *Phys. Status Solidi A* **214**, 1770167 (2017).
14. Yarbrough, W. A. & Messier, R. J. S. Current issues and problems in the chemical vapor deposition of diamond. *Science* **247**, 688–696 (1990).
15. Butler, J. E. & Windischmann, H. Developments in CVD-diamond synthesis during the past decade. *MRS Bull.* **23**, 22–27 (1998).
16. Schwander, M. & Partes, K. J. D. A review of diamond synthesis by CVD processes. *Diam. Relat. Mater.* **20**, 1287–1301 (2011).
17. Linde, O., Geyler, O. & Epstein, A. *The Global Diamond Industry 2018: A Resilient Industry Shines Through* (Bain, 2018).
18. Dossa, S. S. et al. Analysis of the high-pressure high-temperature (HPHT) growth of single crystal diamond. *J. Cryst. Growth* **609**, 127150 (2023).
19. Ferro, S. Synthesis of diamond. *J. Mater. Chem.* **12**, 2843–2855 (2002).
20. Eaton-Magaña, S., Shigley, J. E. & Breeding, C. M. Observations on HPHT-grown synthetic diamonds: a review. *Gems Gemol.* **53**, 262–284 (2017).
21. Sumiya, H., Harano, K. & Tamasaku, K. HPHT synthesis and crystalline quality of large high-quality (001) and (111) diamond crystals. *Diam. Relat. Mater.* **58**, 221–225 (2015).
22. Kalantar-Zadeh, K. et al. Emergence of liquid metals in nanotechnology. *ACS Nano* **13**, 7388–7395 (2019).
23. Taccardi, N. et al. Gallium-rich Pd–Ga phases as supported liquid metal catalysts. *Nat. Chem.* **9**, 862–867 (2017).
24. Daeneke, T. et al. Liquid metals: fundamentals and applications in chemistry. *Chem. Soc. Rev.* **47**, 4073–4111 (2018).
25. Camacho-Mojica, D. C. et al. Charge transfer during the dissociation of H_2 and the charge state of H atoms in liquid gallium. *J. Phys. Chem. C* **123**, 26769–26776 (2019).
26. Ueki, R. et al. *In-situ* observation of surface graphitization of gallium droplet and concentration of carbon in liquid gallium. *Jpn. J. Appl. Phys.* **51**, 06FD28 (2012).
27. Fujita, J.-I. et al. Near room temperature chemical vapor deposition of graphene with diluted methane and molten gallium catalyst. *Sci. Rep.* **7**, 12371 (2017).
28. Upham, D. C. et al. Catalytic molten metals for the direct conversion of methane to hydrogen and separable carbon. *Science* **358**, 917–921 (2017).
29. Allioux, F.-M. et al. Carbonization of low thermal stability polymers at the interface of liquid metals. *Carbon* **171**, 938–945 (2021).
30. Kawasaki, H. et al. A liquid metal catalyst for the conversion of ethanol into graphitic carbon layers under an ultrasonic cavitation field. *Chem. Commun.* **58**, 7741–7744 (2022).
31. Zuraiqi, K. et al. Direct conversion of CO_2 to solid carbon by Ga-based liquid metals. *Energy Environ. Sci.* **15**, 595–600 (2022).
32. Li, P. C. Preparation of single-crystal graphite from melts. *Nature* **192**, 864–865 (1961).
33. Tulloch, H. J. C. & Young, D. A. Synthetic single crystals of graphite. *Nature* **211**, 730–731 (1966).
34. Sumiyoshi, Y., Ushio, M. & Suzuki, S. Formation of graphite single crystal from iron solution by the slow cooling method. *Bull. Chem. Soc. Jpn.* **61**, 1577–1585 (1988).
35. Noda, T., Sumiyoshi, Y. & Ito, N. Growth of single crystals of graphite from a carbon-iron melt. *Carbon* **6**, 813–816 (1968).
36. Austerman, S. B., Myron, S. M. & Wagner, J. W. Growth and characterization of graphite single crystals. *Carbon* **5**, 549–557 (1967).
37. Merel, P., Tabbal, M., Chaker, M., Moisa, S. & Margot, J. Direct evaluation of the sp^3 content in diamond-like-carbon films by XPS. *Appl. Surf. Sci.* **136**, 105–110 (1998).
38. Chu, C., d'Evelyn, M., Hauge, R. & Margrave, J. Mechanism of diamond growth by chemical vapor deposition on diamond (100), (111), and (110) surfaces: carbon-13 studies. *J. Appl. Phys.* **70**, 1695–1705 (1991).
39. Cai, W. et al. Synthesis and solid-state NMR structural characterization of ^{13}C-labeled graphite oxide. *Science* **321**, 1815–1817 (2008).
40. Yang, B. et al. Fabrication of silicon-vacancy color centers in diamond films: tetramethylsilane as a new dopant source. *CrystEngComm* **20**, 1158–1167 (2018).
41. Feng, Z., Lin, Y., Tian, C., Hu, H. & Su, D. Combined study of the ground and excited states in the transformation of nanodiamonds into carbon onions by electron energy-loss spectroscopy. *Sci. Rep.* **9**, 3784 (2019).
42. Luo, K. et al. Coherent interfaces govern direct transformation from graphite to diamond. *Nature* **607**, 486–491 (2022).
43. Tulić, S. et al. Covalent diamond–graphite bonding: mechanism of catalytic transformation. *ACS Nano* **13**, 4621–4630 (2019).
44. Wi, T.-G., Park, Y.-J., Lee, U. & Kang, Y.-B. Methane pyrolysis rate measurement using electromagnetic levitation techniques for turquoise hydrogen production: liquid In, Ga, Bi, Sn, and Cu as catalysts. *Chem. Eng. J.* **460**, 141558 (2023).
45. Gong, Y. et al. Homoepitaxial diamond grown in a liquid metal solvent. *ChemRxiv*. Preprint at https://doi.org/10.26434/chemrxiv-2022-q8ppf (2022).

Methods

Growth of diamonds

An as-received graphite crucible with a 20 mm (length) × 10 mm (width) × 15 mm (depth) cavity in the crucible (Ibiden Ex-60 graphite that was machined by a shop in Korea (GMPI)) was annealed at 1,100 °C in a mixture of H_2 (99.999 at% from KOGAS Tech, 100 sccm) and Ar (from Korea Noble Gas, 99.999 at%, 5 sccm) gas flow at 1 atm pressure for 8 h (Supplementary Fig. 61 and Supplementary Note 3), to remove the impurities; for example, our SEM imaging for runs using the unannealed crucibles showed more metal oxides (particularly aluminium and magnesium). The mixture of Ni ingots (iTASCO, 99.995 wt%), Fe ingots (iTASCO, 99.99 wt%), small pieces broken from a single-crystal Si wafer (Silicon Technology) and liquid gallium (Changsha Rich Nonferrous Metals; 99.9999 wt%) were put into the graphite crucible cavity. EDM-3 Poco Graphite (0.0190-inch-thick; Entegris), HOPG (Grade ZYB; SPI Supplies), or PBN (1-mm thick; MTI Korea) pieces were placed at the bottom of the graphite crucible for some growth runs.

The growth chamber is shown in Supplementary Fig. 1. The graphite crucible is clamped to two water-cooled electrodes inside the chamber of our custom-built cold-wall Joule heating system (the walls are water-jacketed with cooling water flowing between them). The system is connected to gases connected to mass flow controllers and a vacuum system. It is pumped down until the chamber pressure reaches 2 mtorr; the pump is then isolated and 1,000 sccm H_2 flowed until the chamber pressure reaches 760 torr. We then turn on the current to heat the graphite crucible from 25 °C to the growth temperature at a heating rate of 7.7 °C s^{-1}. The temperature at the surface of the centre of the outside of the 'long side' of this graphite crucible was monitored and controlled by a pyrometer (Sensor Therm, Metis M313) with a feedback system that controls the applied current and voltage. (Note that the laser light of the pyrometer was used only during the setup of the position of the pyrometer and the position of the graphite crucible, that is, it was not on during growth). When the temperature read by the pyrometer reached the growth temperature, we changed the H_2 flow rate from 1,000 sccm to 100 sccm and simultaneously flowed 5 sccm CH_4 (from Korea Noble Gas, 99.999 at%). The temperature of the crucible and the flow rates of CH_4 and H_2 were held constant for different growth times; then the current was turned off and the crucible rapidly cooled. A control experiment was done by heating an empty graphite crucible (without the presence of liquid metals) to 1,175 °C (the temperature of the crucible wall reading by pyrometer) under 760 torr of CH_4 (5 sccm) and H_2 (100 sccm) for 150 min showing no diamonds were grown (Supplementary Fig. 62). For ^{13}C-labelling experiments, $^{13}CH_4$ (Cambridge Isotopes Laboratories, CLM-429-PK, 99 at% pure) was used instead of the normal CH_4 mentioned above. For deuterium experiments, D_2 (Korea Noble Gas, 99.999 at% pure) was used instead of the normal H_2 mentioned above.

Diamond film transfer

As-grown diamond film on solidified liquid metal was transferred onto a Cu TEM grid coated with Quantifoil holey amorphous carbon film (R2/1) (SPI Supplies, 300 mesh) for study by TEM and separately onto 300 nm SiO_2/Si wafer pieces for characterization by optical microscopy, AFM, XPS and XRD. Some of the solidified liquid metal pieces after growth were immersed in an 80 °C heated solution of HCl(aq) (35–37%, Daejung Chemicals & Metals). The diamond films detach from the metal surface and go to the bottom of the aqueous HCl solution. We note that only a very small amount of the solidified liquid metal piece needs to be dissolved to free the diamond film regions. Owing to the density of diamond, these sink to the bottom of the HCl(aq) solution. The diamond films were transferred into deionized water. After washing the diamond films three times with deionized water, they were then transferred onto the target substrate, which was then dried at 60 °C in an air oven overnight.

Characterization

The SEM images were obtained with an FEI Verios 460. A Zeiss optical microscope (AxioCam MRc5) was used to acquire the optical images. The AFM data were acquired with a Bruker Dimension Icon system. Synchrotron 2D-XRD pattern in grazing incidence mode of a transferred diamond film on a 300-nm SiO_2/Si wafer was acquired at the PLS-II 6D UNIST-PAL beamline (bending magnet source) of the Pohang Accelerator Laboratory (PAL) using 18.986 keV X-rays. XPS spectra were acquired on the transferred diamond film on the 300-nm SiO_2/Si wafer with a beam size of 200 μm using a Thermo Scientific ESCALAB 250 Xi XPS system equipped with an optical microscope, which was used to locate the beam on the diamond film region. Quenching temperature data were acquired with R-type thermocouples (Supplementary Fig. 3). Visible Raman spectra and UV Raman spectra were obtained using a WITec instrument with 532 nm laser wavelength excitation focused through a 100× objective at 1 mW and 266 nm wavelength laser excitation focused through a 40× objective at 15 mW. UV Raman maps of the as-grown diamond films on the solidified liquid metal surface were acquired with a scan parameter of 1 point per 2 μm over a 50 μm × 50 μm region at 15 mW. Photoluminescence spectra and maps were obtained with this WITec instrument, excited by the 532 nm wavelength laser light focused through a 100× objective. The photoluminescence map of the diamond film was acquired with a scan parameter of 1 point per μm over a 50 μm × 50 μm region. The TEM samples for cross-sectional TEM measurements were prepared using FIB (Helios 450HP SEM-FIB) milling. TEM imaging, TEM-EDS data, EELS spectra and SAED patterns were obtained using an aberration-corrected TEM (FEI Titan G2 60–300) at an acceleration voltage of 80 kV. TOF-SIMS measurements were done with an IONTOF TOF.SIMS 5.

Theoretical simulations

Activation of methane by liquid metals. The calculations were carried out with the Gaussian 09 program. All structures were initially optimized by the density functional theory (DFT) method with the Perdew–Burke–Ernzerhof (PBE) functional. The def2-SVP basis set was used for Ga, Fe and Ni atoms, whereas 6–31 + G(d) was used for the C and H atoms[46]. The vibrational frequencies were calculated at the level of the geometry optimization method. The lowest electronic energy was found by considering different spin states. Electronic energies of relaxed structures were further corrected by single-point calculations using the MP2 level of theory. The Gibbs free energy was computed using the equation: $\Delta G = \Delta E_e + \Delta ZPE + \Delta U - T\Delta S$, where ΔE_e, ΔZPE, ΔU and $T\Delta S$ represent the electronic energy difference, the change in zero-point energy, the thermal energy change and the entropy change, respectively (the temperature (T) was set to 1,300 K). For CH_4 activation on the slab surface (100) of α-Ga, the spin-polarized DFT calculations were conducted using the Vienna Ab initio Simulation Package (VASP)[47]. In the Ga (100) slab, the top two layers were fully relaxed and the bottom two layers were kept fixed. The PBE functional in the generalized gradient approximation was used to describe the exchange-correlation potential[48,49]. A kinetic cutoff energy of 500 eV was set for expanding electronic wave functions. To prevent interactions between periodic images along the z-direction, a 20 Å vacuum was applied. The self-consistent energy convergence and maximum force thresholds were set to 10^{-5} eV and 0.02 eV $Å^{-1}$, respectively. The structures were fully optimized using a 3 × 3 × 1 Monkhorst–Pack grid. The long-range van der Waals interactions were obtained by the Grimme (D3) method[50].

Role of Si. Ab initio molecular dynamics (AIMD)[51–54] using the VASP were performed, with the PBE exchange-correlation potential and a plane wave energy cutoff of 400 eV (refs. 47,49). The initial structure of liquid Ga used a 3 × 2 × 3 supercell using the experimental lattice constant of α-Ga (ref. 55). To achieve the mass density (5.47 g cm^{-3}) of liquid Ga at

1,300 K (ref. 56), the number of Ga atoms was reduced from 144 to 120 and the volume was reduced by 10%. To create a solvent mixture of Ga, Ni and Fe, 13 atoms of Ni and 13 atoms of Fe were added to the 120 Ga atoms while the volume was fixed. For calculating the chemical potentials of C and Si and the formation energies of C_2, Si–C, Si–C–C and C–Si–C, canonical ensemble molecular dynamics (NVT MD) at 1,300 K was performed up to 8 ps at time intervals of 1 fs with the fixed cell volume. When more than five dissolved C or Si were included in the slab, NVT MD was carried out with enough size of vacuum (>12 Å) along the *z*-direction to properly consider the effect of volume. Appropriate initial positions of solvent atoms were obtained by performing pre-molecular dynamics of 0.1 ps when a dimer, trimer or cluster composed of multiple atoms was added with the positions fixed. AIMD was conducted to 5 ps for C_{10} and Si_6C_4, up to 10 ps when carbon was added to Si_6C_4, and over 15 ps for pre-nuclei formation. K-mesh was $1 \times 1 \times 1$ for both three-dimensional periodic bulk and slab structure AIMD, and for DOS and Bader charge, it was $2 \times 2 \times 2$ for bulk and $2 \times 2 \times 1$ for slab. The Grimme's D3 dispersion correction[50] was applied to all bulk and slab calculations. When Ni and Fe are present, the spin of the ferromagnetic alignment is initially assumed for all cases. To obtain the chemical potentials of C and Si, and the formation energies of C_2, Si–C, Si–C–C and C–Si–C, the average value of $E_0 + E_k$ of the last 5,000 steps (5 ps) that achieved sufficient thermal equilibrium was used. Thermal equilibrium was statistically selected when the energy of the last 5,000 steps showed an effect size (Cohen's *d*)[57] smaller than 0.03. The projected DOS and Bader charge of C, Si, C_2, Si–C, Si–C–C and C–Si–C were obtained by averaging the five electronic structures at 6 ps, 6.5 ps, 7 ps, 7.5 ps and 8 ps. In cluster and pre-nucleation simulations, the DOS was calculated for the specified single structure.

Data availability

The published data of this study are available on the Zenodo public database at https://doi.org/10.5281/zenodo.10803625 (ref. 58). Source data are provided with this paper.

46. Ohtsuka, Y. et al. Theoretical study on the C–H activation of methane by liquid metal indium: catalytic activity of small indium clusters. *J. Phys. Chem. A* **123**, 8907–8912 (2019).
47. Kresse, G. & Furthmüller, J. Efficient iterative schemes for *ab initio* total-energy calculations using a plane-wave basis set. *Phys. Rev. B* **54**, 11169–11186 (1996).
48. Perdew, J. P., Burke, K. & Ernzerhof, M. Perdew, Burke, and Ernzerhof reply. *Phys. Rev. Lett.* **80**, 891 (1998).
49. Perdew, J. P., Burke, K. & Ernzerhof, M. Generalized gradient approximation made simple. *Phys. Rev. Lett.* **77**, 3865–3868 (1996).
50. Grimme, S., Antony, J., Ehrlich, S. & Krieg, H. A consistent and accurate *ab initio* parametrization of density functional dispersion correction (DFT-D) for the 94 elements H-Pu. *J. Chem. Phys.* **132**, 154104 (2010).
51. Nosé, S. A unified formulation of the constant temperature molecular dynamics methods. *J. Chem. Phys.* **81**, 511–519 (1984).
52. Nose, S. Constant-temperature molecular dynamics. *J. Phys. Condens. Matter* **2**, SA115 (1990).
53. Hoover, W. G. Canonical dynamics: equilibrium phase-space distributions. *Phys. Rev. A* **31**, 1695–1697 (1985).
54. Frenkel, D. & Smit, B. *Understanding Molecular Simulation: From Algorithms to Applications* (Academic Press, 1996).
55. Sharma, B. D. & Donohue, J. A refinement of the crystal structure of gallium. *Z. Kristallogr. Cryst. Mater.* **117**, 293–300 (1962).
56. Assael, M. J. et al. Reference data for the density and viscosity of liquid cadmium, cobalt, gallium, indium, mercury, silicon, thallium, and zinc. *J. Phys. Chem. Ref. Data* **41**, 033101 (2012).
57. Cohen, J. *Statistical Power Analysis for the Behavioral Sciences* (Academic Press, 2013).
58. Yan, G., Da, L. & Rodney, R. Source data for "Growth of diamond in liquid metal at 1 atmosphere pressure". *Zenodo* https://doi.org/10.5281/zenodo.10803625 (2024).

Acknowledgements This work was supported by the Institute for Basic Science (IBS-R019-D1). We thank S. Y. Lee for preliminary XRD measurements at the 9C beamline of Pohang Accelerator Laboratory to evaluate the crystalline property of the diamond sample, and B. Cunning for suggesting the EDM-3 Poco Graphite sheet material and for discussions. The experiments at the PLS-II 6D and 9C beamline were supported in part by MSIT, POSTECH and UNIST Central Research Facilities. We thank K.-S. Lee of the UNIST Center Research Facilities for making the TOF-SIMS measurements. The DFT calculations were conducted on the IBS supercomputer.

Author contributions R.S.R. supervised the project. R.S.R., D.L. and Y.G. conceived the experiments. Y.G. did the growth experiments. Y.G. and D.L. characterized the diamond samples. W.K.S. designed, assembled and built, and tested the cold-wall system and the thermocouple probe array. M.C. and Z.L. took the TEM, STEM, EELS and EDS measurements. P.B. took the XPS measurements. T.J.S. and S.L. took the XRD measurements. Y.K., B.R., M.Z., I.K.P. and G.L. performed the theoretical calculations. M.W. contributed through discussion. Y.G. wrote a draft manuscript and R.S.R., D.L. and Y.G. revised it. All co-authors commented on the manuscript before its submission.

Competing interests The Institute for Basic Science has filed a patent application (KR 10-2023-0052752) that lists Y.G., D.L. and R.S.R. as inventors. Other than this, the authors declare no competing interests.

Additional information

Supplementary information The online version contains supplementary material available at https://doi.org/10.1038/s41586-024-07339-7.

Correspondence and requests for materials should be addressed to Da Luo, Won Kyung Seong or Rodney S. Ruoff.

Peer review information *Nature* thanks Anirudha Sumant and the other, anonymous, reviewer(s) for their contribution to the peer review of this work. Peer reviewer reports are available.